POLITECNICO DI TORINO
Repository ISTITUZIONALE

Excitons and light-emission in semiconducting MoSi2X4 two-dimensional materials

Original
Excitons and light-emission in semiconducting MoSi2X4 two-dimensional materials / Sun, Ml; Re Fiorentin, M; Schwingenschlogl, U; Palummo, M. - In: NPJ 2D MATERIALS AND APPLICATIONS. - ISSN 2397-7132. - ELETTRONICO. - 6:1(2022). [10.1038/s41699-022-00355-z]

Availability:
This version is available at: 11583/2974212 since: 2023-01-12T16:33:50Z

Publisher:
NATURE PORTFOLIO

Published
DOI:10.1038/s41699-022-00355-z

Terms of use:

This article is made available under terms and conditions as specified in the corresponding bibliographic description in the repository

Publisher copyright

(Article begins on next page)

24 April 2024

npj | 2D materials and applications

www.nature.com/npj2dmaterials

ARTICLE OPEN

Excitons and light-emission in semiconducting $MoSi_2X_4$ two-dimensional materials

Minglei Sun[1,4], Michele Re Fiorentin[2,4], Udo Schwingenschlögl[1]✉ and Maurizia Palummo[3]✉

Semiconducting two-dimensional materials with chemical formula $MoSi_2X_4$ (X = N, P, or As) are studied by means of atomistic ground- and excited-state first-principles simulations. Full-fledged quasi-particle bandstructures within the G_0W_0 approach substantially correct the electronic bandgaps previously obtained with hybrid-functional density functional theory and highlight the absence of lateral valleys close in energy to the conduction band minimum. By solving the Bethe–Salpeter equation, we show that the optical properties are dominated by strongly bound excitons with the absorbance and maximum short-circuit current densities of $MoSi_2P_4$ and $MoSi_2As_4$ comparable to those of transition metal dichalcogenides. Due to the presence of the outer SiX layers, the exciton binding energies are smaller than those generally found for transition metal dichalcogenides. Long radiative lifetimes of bright excitons, over 10 ns at room temperature for $MoSi_2As_4$, and the absence of band-nesting are very promising for application in efficient ultra-thin optoelectronic devices.

npj 2D Materials and Applications (2022)6:81 ; https://doi.org/10.1038/s41699-022-00355-z

INTRODUCTION

Atomically thin two-dimensional (2D) materials are nowadays the subject of intense fundamental and technological research[1–6]. Due to the reduced dimensionality and the weak dielectric screening, their opto-electronic response, even at room temperature, is dominated by strongly bound electron-hole pairs, called excitons[7]. Among a plethora of semiconducting 2D materials, the family of group VI transition metal dichalcogenides (TMDs) is most attractive for very high absorbance and optical bandgaps ranging from the visible to the near-infrared region of the electromagnetic spectrum[8,9]. TMDs thus are promising candidates for next generation opto-electronic and photonic devices, such as photovoltaic solar cells[10,11], photodetectors[12,13], and light-emitting diodes[14]. However, the opto-electronic performance of TMDs is affected by spin and momentum-forbidden dark excitons. The former originate from the strong spin-orbit coupling at the K and K′ points[15,16], the latter are mainly due to the presence of lateral valleys at the Λ (or Q) point, midway between the Γ and K points of the Brillouin zone[17]. Their energy ordering relative to the bright direct K-K excitons has a profound impact on the photoluminescence efficiency. A spin-forbidden dark exciton as lowest-energy state, as in WS_2, and finite momentum excitons energetically close to the bright exciton, as in MoS_2, introduce additional non-radiative decay channels that hamper the photoluminescence quantum yield[17].

The 2D semiconducting material $MoSi_2N_4$ recently has been synthesized by chemical vapor deposition[18]. It has a layered structure with $P\bar{6}m2$ space group, in which an inner MoN_2 layer is coordinated to two outer SiN layers, compare Fig. 1. It exhibits an indirect band gap, a high strength (66 GPa), and remarkable ambient stability. Theoretical calculations based on the deformation potential approach predict high intrinsic electron and hole mobilities of $270\,cm^2V^{-1}s^{-1}$ and $1200\,cm^2V^{-1}s^{-1}$, respectively[18,19], which result in a high on/off ratio of 4000 at 77 K in a back-gated field-effect transistor. The carrier type and bandgap of $MoSi_2N_4$ can be easily manipulated by doping[20]. Interestingly, other 2D materials with the general formula $MoSi_2X_4$ and the same structure as $MoSi_2N_4$ can be obtained by elemental substitution and exhibit versatile properties[21]. The indirect bandgap becomes direct after replacing the N atoms by P or As atoms[22,23]. The absence of inversion symmetry in the structure of $MoSi_2X_4$ allows for valley polarization by optical pumping with circularly polarized light[22,24], making the materials suitable for application in spintronics and valleytronics[21]. Several members of the family exhibit high piezoelectric coefficients and are predicted to show high lattice thermal conductivity, comparable with Cu[25].

Despite the appeal of the materials, theoretical investigations in the literature have focused on the electronic and optical properties[22,26,27] mainly within the limited density functional theory (DFT) approach. It is known that DFT fails at properly predicting both the electronic bandgap of semiconductors and the light absorption spectra. In particular, DFT intrinsically misses the excitonic features that are essential in low-dimensional materials. For this reason, in this work, we study $MoSi_2X_4$ (X = N, P, or As) employing state-of-the-art many-body perturbation theory techniques, to disclose the excitonic nature of the optical properties, which inevitably must be taken into account to provide thorough insights into the basic properties of these materials and reliable guidance to future experimental works.

RESULTS AND DISCUSSION

Structure and electronic properties

Figure 1 shows the relaxed atomic structures of $MoSi_2N_4$, $MoSi_2P_4$, and $MoSi_2As_4$. Their optimized lattice constants are 2.91, 3.47, and 3.62 Å, respectively, in agreement with previous reports[18,27]. The PBE and G_0W_0 band structures are reported in Fig. 2. We confirm that $MoSi_2N_4$ is an indirect bandgap semiconductor both at the PBE and G_0W_0 levels, with the valence band maximum (VBM) located at the Γ point and the conduction band minimum (CBM)

[1]Applied Physics Program, Physical Science and Engineering Division, King Abdullah University of Science and Technology (KAUST), Thuwal, Saudi Arabia. [2]Center for Sustainable Future Technologies, Istituto Italiano di Tecnologia, Torino, Italy. [3]Dipartimento di Fisica and INFN, Università di Roma "Tor Vergata", Roma, Italy. [4]These authors contributed equally: Minglei Sun, Michele Re Fiorentin. ✉email: udo.schwingenschlogl@kaust.edu.sa; maurizia.palummo@roma2.infn.it

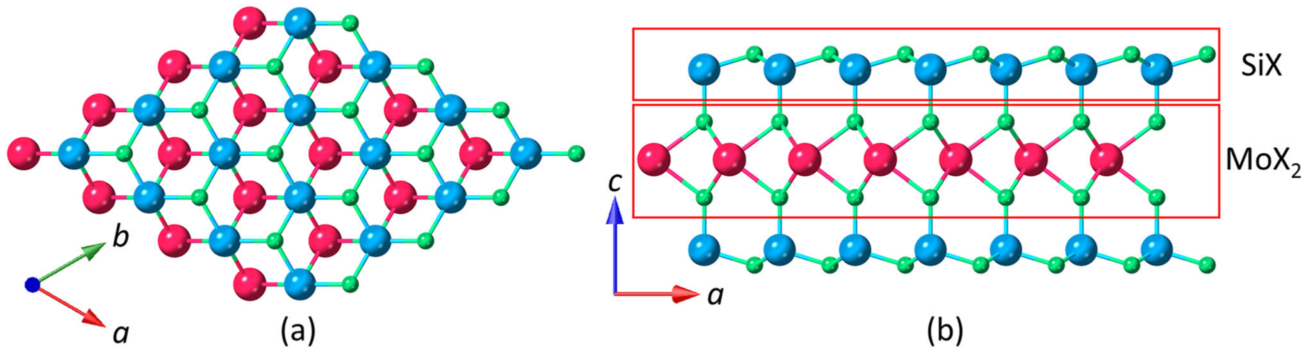

Fig. 1 Atomic structure. Top **a** and side **b** views. In **b** the MoX_2 and SiX layers are marked. The violet, blue, and green spheres are Mo, Si, and X atoms, respectively.

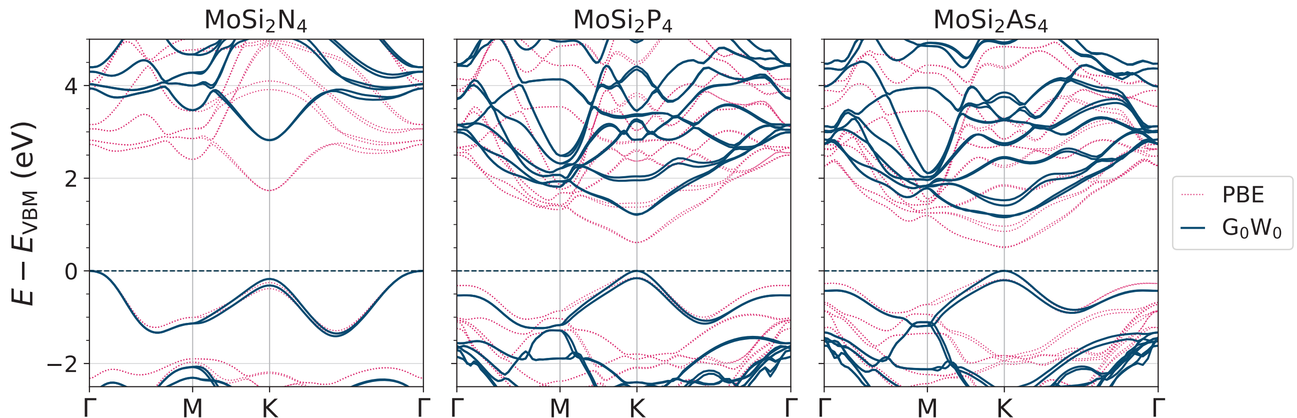

Fig. 2 Band structures. The energies refer to the VBM.

located at the K point. Both the valence and conduction band edges are split due to spin-orbit coupling and lack of inversion symmetry. The valence band edge at the K point shows a splitting of 158 (141) meV at the G_0W_0 (PBE) level, while the conduction band edge shows a much smaller splitting of 10 (3) meV. The G_0W_0 bandgap is 2.79 eV, i.e., 1.02 eV larger than the PBE bandgap. The direct gap at the K point is 2.96 eV, i.e., 0.18 eV larger than the indirect bandgap. In $MoSi_2P_4$ and $MoSi_2As_4$ the bandgaps turn direct with the VBM shifting to the K point. The splittings at the VBM and CBM are much larger than for $MoSi_2N_4$, specifically, 158 (139) and 14 (4) meV for $MoSi_2P_4$ and 203 (181) and 28 (16) meV for $MoSi_2As_4$ at the G_0W_0 (PBE) level due to the heavier masses of P and As. The G_0W_0 bandgap is 1.17 eV for $MoSi_2P_4$ and 1.01 eV for $MoSi_2As_4$. As a comparison, the HSE06 hybrid functional[27] underestimates the direct bandgap with respect to the G_0W_0 bandgap by about 0.35 eV for $MoSi_2P_4$ and $MoSi_2As_4$ and by 0.65 eV for $MoSi_2N_4$. This fact has sizeable implications on the optical properties of the materials. It is worth mentioning that the G_0W_0 bandgaps of $MoSi_2X_4$ are inversely proportional to the atomic number of the X element, as explained by the decreasing electronegativity.

Figure 2 also displays a first significant difference from traditional TMDs. The absence of lateral valleys (e.g., the Λ valleys in TMDs) along the Γ-K high-symmetry direction. Due to the absence of Λ valleys close in energy to the K valleys, excitons have fewer non-radiative recombination channels in $MoSi_2X_4$ than in TMDs, hinting at a less suppressed quantum yield and high efficiencies in optoelectronic devices. It recently has been proven that non-radiative recombination channels can be efficiently suppressed in TMDs by electrostatic doping[28] and strain[29]. We anticipate that the same approaches can be applied to further enhance the quantum yield of $MoSi_2X_4$ (X = N, P, or As).

Optical properties

In the upper panels of Fig. 3 we report the absorption spectra computed at the BSE level. The absorption onset falls in the visible region for $MoSi_2N_4$, at 2.31 eV, and in the near infrared region at 0.77 and 0.71 eV for $MoSi_2P_4$ and $MoSi_2As_4$, respectively. The overlap of the absorption spectra with the incident AM1.5G solar flux $\Phi_s(\omega)$ (shaded gray region in Fig. 3), while limited for $MoSi_2N_4$, is larger for $MoSi_2P_4$ and $MoSi_2As_4$. To quantify the theoretical efficiency of the absorption of solar light we compute the maximum short-circuit current density as $J_{sc}^{max} = e\int d\omega A(\omega)\Phi_s(\omega)$, where $A(\omega)$ is the absorbance[11]. The value of J_{sc}^{max} is only 0.7 mA/cm^2 in the case of $MoSi_2N_4$, while $MoSi_2P_4$ and $MoSi_2As_4$ exhibit large values of 3.6 and 4.5 mA/cm^2, respectively, because of the lower absorption onset. These values are comparable with well-studied TMDs[30], such as MoS_2 (3.9 mA/cm^2) and $MoSe_2$ (4.6 mA/cm^2), indicating great potential of $MoSi_2X_4$ in photovoltaic applications.

Exciton fine structure

Selected absorption peaks A, B, $\widetilde{B}$, and C are marked in the upper panels of Fig. 3, with the electronic transitions taking place at the *k*-points correspondingly highlighted in the lower panels. Similarly to TMDs, peaks A and B are due to well-defined excitons with contributions from transitions at the K and K′ points, reflecting the band splitting induced by the spin-orbit coupling. As shown in more detail for $MoSi_2P_4$ in Fig. 4a–c, excitons A and B originate

Published in partnership with FCT NOVA with the support of E-MRS

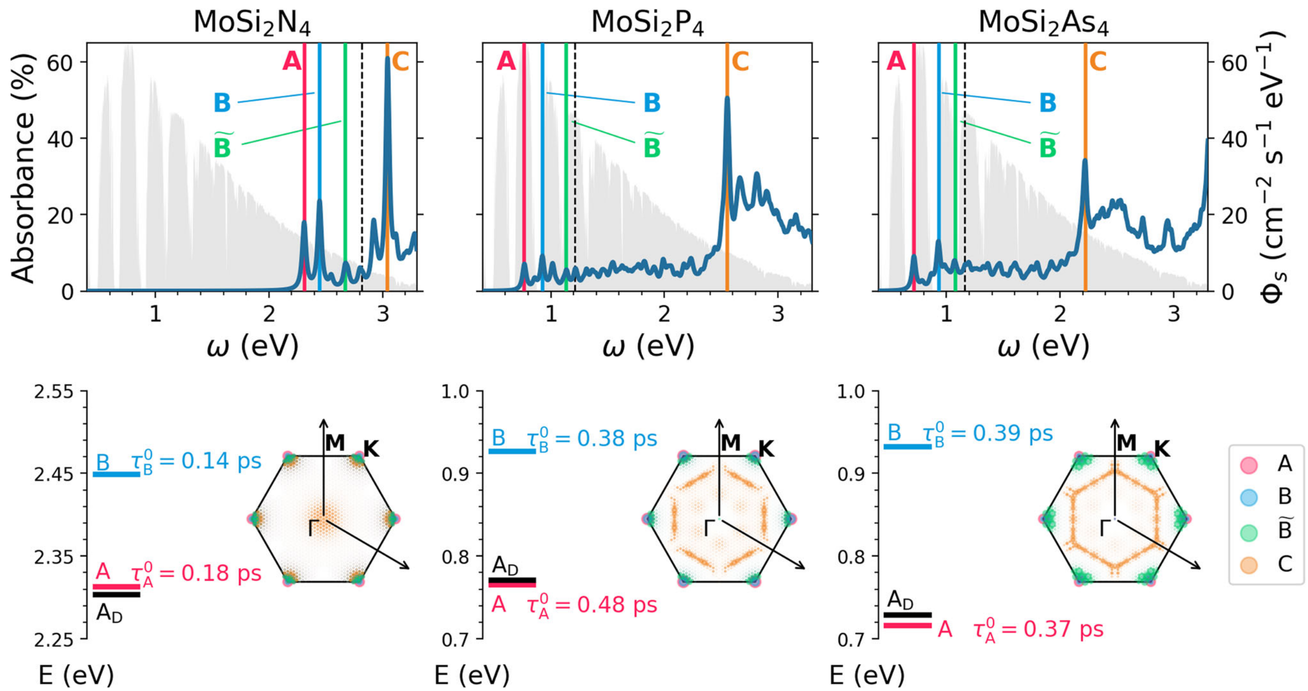

Fig. 3 Absorption spectra and exciton radiative lifetimes. Upper panels: Absorption spectra computed at the BSE level. The dashed vertical lines mark the G_0W_0 bandgaps. Lower panels: Intrinsic radiative lifetimes of excitons A and B at 0 K, and exciton weights in the Brillouin zone. A_D denotes the dark exciton.

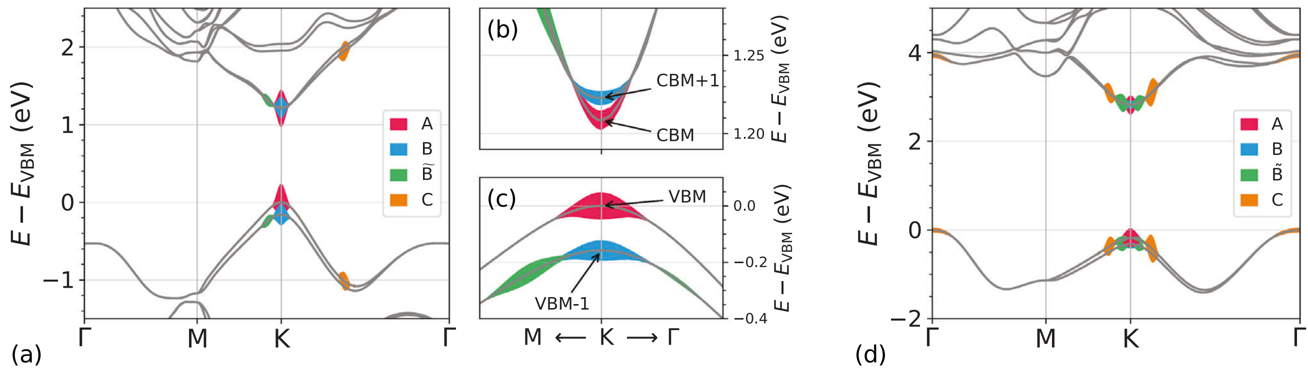

Fig. 4 Weighted band structures. G_0W_0 bandstructure of **a** $MoSi_2P_4$ and **d** $MoSi_2N_4$ with weights of the single-particle transitions giving rise to excitons A, B, $\widetilde{B}$, and C (Fig. 3). In **b** and **c** we report details of the CBM(+1) and VBM(−1), respectively, around the K point.

from the allowed transitions between same-spin bands, namely VBM → CBM for exciton A and VBM−1 → CBM+1 for exciton B. The binding energy of exciton A is 0.68 eV in $MoSi_2N_4$ and 0.44 eV in both $MoSi_2P_4$ and $MoSi_2As_4$, i.e., smaller than the binding energy of the lowest-energy bright exciton of a MoS_2 monolayer, estimated to be larger than 0.70 eV at the same level of theory[31,32]. Excitons A and B in the case of $MoSi_2N_4$ are located at 2.31 and 2.45 eV, respectively, in agreement with the experimental values (2.21 and 2.35 eV)[18]. The 0.1 eV blueshift of the computed exciton energies with respect to the experimental values can be attributed to three main effects that were not included in the calculations: the presence of a substrate, which has been shown to reduce the optical gap of single-layer TMDs by up to 0.1 eV[33,34], temperature effects, which already at 0 K cause a redshift of 75 meV in single-layer MoS_2 due to zero-point renormalization[35], and tensile strain, which has a strong impact on the band structure of $MoSi_2N_4$ already at small magnitudes (see Supplementary Fig. 4).

Spin-forbidden transitions between opposite-spin bands at the K and K′ points give rise to the dark exciton A_D with zero dipole moment for in-plane light polarization. Above peaks A and B, it is possible to identify in Fig. 3 several peaks with lower intensities. As a representative, we select a peak $\widetilde{B}$, which is due to VBM−1 → CBM+1 transitions (as peak B) taking place near the K and K′ points (Fig. 4). These transitions are slightly more energetic and less intense, as they occur only in the vicinity of the high-symmetry K and K′ points.

Finally, we find in Fig. 3 an intense absorption peak at higher energy, well above the G_0W_0 direct bandgap, which originates from direct transitions (VBM → CBM) within the Brillouin zone (lower panels of Fig. 3). We mark it as C to suggest a possible analogy with the intense peaks that are found in TMDs and are mainly given by similar transitions at *k*-points intermediate between Γ and K. In the case of the TMDs these transitions take place in regions of the Brillouin zone where the valence and conduction bands are almost parallel, i.e., 'nested'[36]. In such

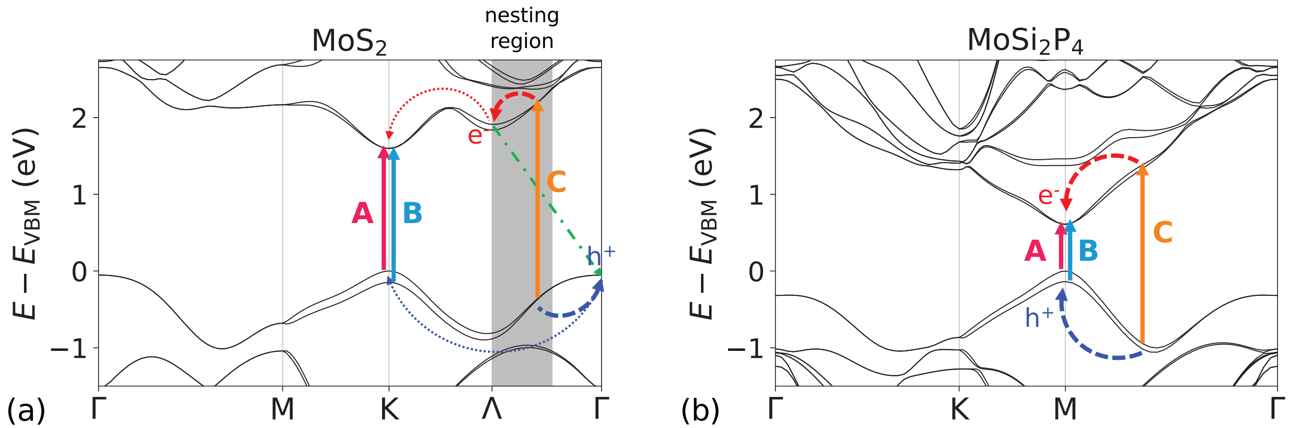

Fig. 5 Relaxation. Relaxation processes of the excited charge carriers from peak C in **a** MoS_2 and **b** $MoSi_2P_4$.

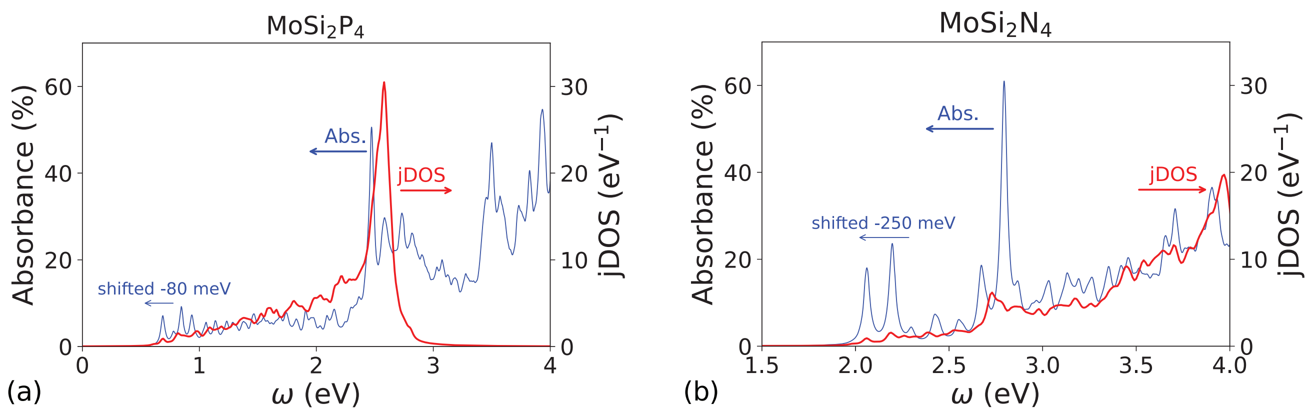

Fig. 6 jDOS and absorbance. jDOS per unit cell (red line) and absorbance (blue line) of **a** $MoSi_2P_4$ and **b** $MoSi_2N_4$. The jDOS is obtained from the PBE eigenvalues and only comprises transitions involving the VBM−1, VBM, CBM, and CBM+1. The absorbance is shifted to match the jDOS, as reported in each panel.

conditions, photo-generated electrons and holes relax with opposite momenta to their closest band extrema, i.e., to the Λ valley and Γ hill, respectively. Hence, photo-generated carriers remain separated in momentum space, and the quantum yield drops significantly[37]. This does not happen for $MoSi_2P_4$ and $MoSi_2As_4$ according to Fig. 4, since no lateral valley is interposed between the transitions and the band extrema at the K and K′ points. In Fig. 5 we show a schematic of the electron-hole relaxation mechanisms in (a) MoS_2 and (b) $MoSi_2P_4$. In MoS_2 the excited electrons from peak C quickly relax via intraband scattering to the Λ valley between the Γ and K points (dashed red arrow). Simultaneously, the excited holes relax to the Γ hill (blue dashed arrow). Once relaxed, the charge carriers can follow phonon-mediated radiative recombination (dot-dashed green arrow), or non-radiative recombination, or phonon scattering to the K and K′ points (dotted red and blue arrows). Only a relatively small fraction of the photo-excited carriers reaches the K and K′ points and recombines radiatively, with moderate yield[37]. In the cases of $MoSi_2P_4$ and $MoSi_2As_4$, see Fig. 5b, the photo-generated electrons and holes are statistically favored to quickly relax to the closest K or K′ points, via interband scattering (red and blue dashed arrows). It is not possible to fully exclude relaxation paths leading holes to the Γ hill, however they are disfavored by the longer interband scattering chain.

Band nesting in TMDs results in a large enhancement of the joint density of states (jDOS) and, in turn, in an increased absorbance. In $MoSi_2P_4$ and $MoSi_2As_4$ the large intensity of peak C can be similarly traced back to the jDOS, see Fig. 6a. However, this enhancement is not related to band nesting, see Fig. 4, but rather to the reduced curvature of the valence and conduction bands in the region where the electronic transitions contributing to peak C occur. In $MoSi_2N_4$ the intense peak C is mainly due to contributions from electronic transitions in the vicinity of K/K′, as well as at Γ (see the lower panels of Figs. 3 and 4d). The band structure of $MoSi_2N_4$ shows flat conduction and valence bands around Γ, which enhance the jDOS and, consequently, the intensity, see Fig. 6b. This feature is absent in $MoSi_2P_4$ and $MoSi_2As_4$.

As mentioned, the energetic ordering of excitons A_D and A is crucial for the optoelectronic performance. We have verified that in our calculations the bright-dark splitting $\Delta \equiv E_A - E_{A_D}$ is converged within 2 meV (see Supplementary Fig. 2c). It is important to notice that, while in the case of $MoSi_2N_4$ the dark exciton A_D is the lowest-energy state, with a bright-dark splitting $\Delta = 9$ meV, the ordering is reversed in the cases of $MoSi_2P_4$ and of $MoSi_2As_4$, where we have $\Delta = -3$ and -13 meV, respectively (lower panels of Fig. 3). This is the result of interplay between the splitting of the conduction band due to the spin-orbit coupling and the exchange interaction between the electron and hole in the exciton[32,38]. Indeed, in all three studied materials the band splitting provides a negative contribution to Δ, since the opposite-spin bands involved in exciton A_D are the VBM and CBM+1, implying that the electronic transitions contributing to exciton A (VBM → CBM) are less energetic than those contributing to exciton A_D. On the contrary, the exchange interaction always contributes positively to Δ, lowering the energy of the dark exciton with

respect to the bright exciton. The contribution of the exchange interaction to Δ is found to be between 12 meV ($MoSi_2P_4$) and 18 meV ($MoSi_2N_4$), being large enough to overcome the band splitting due to the spin-orbit coupling only in the case of $MoSi_2N_4$ (positive Δ). The negative Δ implies that $MoSi_2P_4$ and $MoSi_2As_4$ will show an enhanced quantum yield at low temperatures, unlike TMDs such as WS_2, WSe_2[39], and MoS_2[40,41]. In the case of $MoSi_2As_4$, due to the large $\Delta = -13$ meV, the quantum yield is expected to be only moderately suppressed even at room temperature, unlike $MoSe_2$ with $\Delta = -1$ meV[16,42]. The energetic ordering of the excitons and bright-dark splitting represent the second main specificity of the materials under consideration with respect to traditional TMDs.

The lower panels of Fig. 3 also give the intrinsic radiative lifetimes of excitons A and B at 0 K, $\tau^0_{A,B}$, which all fall in the range of tenths of ps, in line with the values obtained for 2D TMDs[43]. As shown in Refs. [43–45], in a 2D material the finite temperature radiative lifetime $\langle\tau_X\rangle(T)$ of exciton X is proportional to $k_B T M^*_X / E^2_X$, where M^*_X and E_X are the effective mass and energy of the exciton at zero momentum, respectively. We report in Table 1 the effective masses of the electrons, holes, and excitons, together with the finite temperature exciton radiative lifetimes calculated at $T = 4$ and 300 K.

The values obtained for $MoSi_2N_4$ are slightly larger than those of MoS_2, $MoSe_2$, and WSe_2[46]. Conversely, the values obtained for $MoSi_2P_4$ and $MoSi_2As_4$ are about two orders of magnitude larger. This is primarily due to the combination of low energy ($E_{A,B} < 1$ eV) and high effective mass of the excitons, which enhances the temperature-dependent factor in $\langle\tau\rangle(T)$. Long radiative lifetimes are often associated with exciton localization due to defects or strain, as observed for TMD monolayers and bilayers[47,48], or with interlayer excitons in 2D van der Waals heterostructures of TMDs[49–51].

Table 1. Effective exciton masses and finite temperature radiative lifetimes.

	$MoSi_2N_4$		$MoSi_2P_4$		$MoSi_2As_4$	
	A	B	A	B	A	B
$M^*(m_0)$	0.79	1.30	0.47	1.05	1.94	1.12
$m^*_e(m_0)$	0.28	0.74	0.18	0.69	1.51	0.58
$m^*_h(m_0)$	0.51	0.56	0.29	0.36	0.42	0.54
$\langle\tau\rangle$ (4 K) (ps)	7	8	100	123	372	133
$\langle\tau\rangle$ (300 K) (ns)	1	1	7	9	28	10

The effective exciton masses are obtained from the G_0W_0 bandstructure and reported in units of the electron rest mass m_0. The finite temperature radiative lifetimes are computed for excitons A and B at 4 and 300 K.

We plot in Fig. 7 the square moduli of the wavefunctions of excitons A, B, $\tilde{B}$, and C of $MoSi_2P_4$. Corresponding results for $MoSi_2N_4$ and $MoSi_2As_4$ are reported in Supplementary Figs. 5 and 6, respectively. The hole (white diamond) is kept fixed where the valence band edge has the highest probability density. In all cases, excitons A and B both have a circular shape around the hole. The Bohr radii of excitons A and B are estimated to be, respectively, $a_A = 1.79$ nm and $a_B = 1.76$ nm in $MoSi_2P_4$, 0.98 nm and 0.96 nm in $MoSi_2N_4$, and 1.65 nm and 1.64 nm in $MoSi_2As_4$, in line with the values found in TMDs[52–54]. Exciton $\tilde{B}$ is more delocalized, and exciton C spreads along the zigzag direction. The side views in Fig. 7 show that excitons A, B, and $\tilde{B}$ are concentrated on the inner $MoSi_2$ layer, whereas exciton C extends to the outer SiP layers. Exciton C shows a similar delocalization in $MoSi_2As_4$, while it does not extend to the outer SiN layers in $MoSi_2N_4$.

Exciton-exciton annihilation (strong exciton Auger recombination) is a key technological bottleneck to obtain high quantum yield in TMDs, and the less localized C exciton may enhance the annihilation rate by increasing the annihilation radius[55–57]. Lee et al.[58] have employed ultra-flat Au substrates with atomically controlled h-BN spacers to suppress the exciton-exciton interaction and improve the quantum yield of TMDs by an order of magnitude. In $MoSi_2X_4$ layers, due to the contribution of the excitons in the inner MoX_2 layer, the outer SiX layers can act as the h-BN spacers. Thus, chemical vapor deposition of $MoSi_2X_4$ on a metallic substrate may directly lead to highly efficient optoelectronic devices.

We provide a state-of-the-art study of the electronic and optical properties of 2D $MoSi_2X_4$ based on many-body perturbation theory. The G_0W_0 approximation overcomes the drawbacks of DFT, being superior to hybrid-functionals, to achieve reliable electronic band structures and bandgaps. The bandgap of $MoSi_2N_4$ is indirect, while the bandgaps of $MoSi_2P_4$ and $MoSi_2As_4$ are direct at the K point with a bandgap value of around 1 eV. Unlike traditional TMDs, they have no lateral valleys close in energy to the CBM. By solving the Bethe-Salpeter equation, we obtain absorption spectra displaying excitonic features. The absorption onset falls into the visible region for $MoSi_2N_4$, and into the near-infrared region for $MoSi_2P_4$ and $MoSi_2As_4$, resulting, together with a strong light-carrier coupling, in a significant absorption of the solar flux and in maximum short-circuit current densities comparable to those of TMDs. The analysis of the exciton fine-structure reveals a crucial interplay between the band splitting induced by the spin-orbit coupling and the exchange interaction within the exciton, which results in a bright lowest-

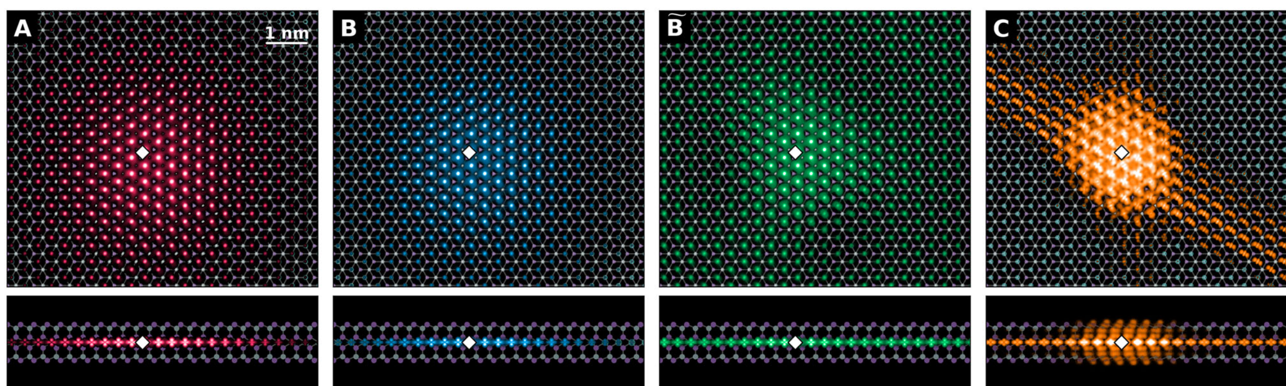

Fig. 7 Wavefunctions. Top (upper panels) and side (lower panels) views of the square moduli of the wavefunctions of excitons A, B, $\tilde{B}$, and C in $MoSi_2P_4$. The white diamond marks the highest probability density of the hole.

energy exciton for both $MoSi_2P_4$ and $MoSi_2As_4$. The negative bright-dark splitting is particularly large (−13 meV) for $MoSi_2As_4$. Our detailed analysis suggests that the materials under investigation provide remarkable quantum yields, especially $MoSi_2As_4$. Absence of lateral valleys, negative bright-dark splitting, and long exciton radiative lifetime give rise to high performance optoelectronic materials.

METHODS

We perform DFT calculations within the plane-wave expansion using the Quantum Espresso package[59]. The gradient-corrected Perdew–Burke–Ernzerhof (PBE) functional[60] is employed together with fully relativistic norm-conserving pseudopotentials[61] that account for the spin-orbit coupling. We consider as semicore states the Mo 4s and 4p orbitals, as well as the As 3d orbitals. Convergence is achieved with an 80 Ry kinetic energy cutoff and a uniform $24 \times 24 \times 1$ Monkhorst-Pack *k*-point mesh[62]. A 15 Å vacuum region along the *c*-direction, the direction perpendicular to the layer plane, is introduced to ensure decoupling of periodic replicas. The structure relaxation is assumed to have reached convergence when the maximum component of the residual ionic forces is smaller than 10^{-8} Ry/Bohr.

Building up on the obtained DFT results, we perform many-body perturbation theory calculations within the G_0W_0 approximation using the Yambo code[63,64]. A box cutoff along the *c*-direction is applied to the bare Coulomb potential. The inverse dielectric matrix, $\varepsilon^{-1}_{\mathbf{GG}'}$, is obtained within the plasmon-pole approximation[64]. We adopt the quasiparticle bandgap value at the K point as convergence parameter and fix a convergence threshold of 50 meV. Following this criterion, we employ a $36 \times 36 \times 1$ k-point mesh, 300 bands and a 10 Ry cutoff for the **G** vectors in $\varepsilon^{-1}_{\mathbf{GG}'}$ and 240 bands for the computation of the correlation self-energy. In order to speed up the convergence with respect to empty states we adopted the technique described in Ref. [65] as implemented in the Yambo code[64].

The quasiparticle band structures are then used to build and solve the Bethe-Salpeter equation on a $36 \times 36 \times 1$ k-point mesh, including eight valence and ten conduction bands in the excitonic Hamiltonian (compare the Supplementary Information).

DATA AVAILABILITY

The data supporting the findings of this study are available within the article.

CODE AVAILABILITY

No custom code is used.

Received: 29 April 2022; Accepted: 14 October 2022;
Published online: 07 November 2022

REFERENCES

1. Novoselov, K. S. et al. Two-dimensional atomic crystals. *Proc. Natl Acad. Sci. USA* **102**, 10451–10453 (2005).
2. Geim, A. K. & Grigorieva, I. V. Van der Waals heterostructures. *Nature* **499**, 419–425 (2013).
3. Bhimanapati, G. R. et al. Recent advances in two-dimensional materials beyond graphene. *ACS Nano* **9**, 11509–11539 (2015).
4. Tan, T., Jiang, X., Wang, C., Yao, B. & Zhang, H. 2d material optoelectronics for information functional device applications: status and challenges. *Adv. Sci.* **7**, 2000058 (2020).
5. Kang, S. et al. 2d semiconducting materials for electronic and optoelectronic applications: potential and challenge. *2D Mater.* **7**, 022003 (2020).
6. Bernardi, M., Ataca, C., Palummo, M. & Grossman, J. Electronic properties of two-dimensional layered materials. *Nanophotonics* **6**, 479–493 (2016).
7. Zheng, X. & Zhang, X. Excitons in two-dimensional materials. In Thirumalai, J. & Pokutnyi, S. I. (eds.) *Advances in Condensed-Matter and Materials Physics*, chap. 2 (IntechOpen, Rijeka, 2020).
8. Rasmussen, F. A. & Thygesen, K. S. Computational 2d materials database: Electronic structure of transition-metal dichalcogenides and oxides. *J. Phys. Chem. C* **119**, 13169–13183 (2015).
9. Manzeli, S., Ovchinnikov, D., Pasquier, D., Yazyev, O. V. & Kis, A. 2d transition metal dichalcogenides. *Nat. Rev. Mater.* **2**, 17033 (2017).
10. Nassiri Nazif, K. et al. High-specific-power flexible transition metal dichalcogenide solar cells. *Nat. Commun.* **12**, 7034 (2021).
11. Bastonero, L., Cicero, G., Palummo, M. & Re Fiorentin, M. Boosted solar light absorbance in PdS_2/PtS_2 vertical heterostructures for ultrathin photovoltaic devices. *ACS Appl. Mater. Interfaces* **13**, 43615–43621 (2021).
12. Zha, J. et al. Infrared photodetectors based on 2d materials and nanophotonics. *Adv. Funct. Mater.* **32**, 2111970 (2022).
13. Taffelli, A., Diré, S., Quaranta, A. & Pancheri, L. MoS_2 based photodetectors: a review. *Sensors* **21**, 2758 (2021).
14. Wang, C., Yang, F. & Gao, Y. The highly-efficient light-emitting diodes based on transition metal dichalcogenides: from architecture to performance. *Nanoscale Adv.* **2**, 4323–4340 (2020).
15. Mueller, T. & Malic, E. Exciton physics and device application of two-dimensional transition metal dichalcogenide semiconductors. *npj 2D Mater. Appl.* **2**, 29 (2018).
16. Robert, C. et al. Measurement of the spin-forbidden dark excitons in MoS_2 and $MoSe_2$ monolayers. *Nat. Commun.* **11**, 4037 (2020).
17. Malic, E. et al. Dark excitons in transition metal dichalcogenides. *Phys. Rev. Mater.* **2**, 014002 (2018).
18. Hong, Y.-L. et al. Chemical vapor deposition of layered two-dimensional $MoSi_2N_4$ materials. *Science* **369**, 670–674 (2020).
19. Jian, C.-C., Ma, X., Zhang, J. & Yong, X. Strained $MoSi_2N_4$ monolayers with excellent solar energy absorption and carrier transport properties. *J. Phys. Chem. C* **125**, 15185–15193 (2021).
20. Abdelati, M. A., Maarouf, A. A. & Fadlallah, M. M. Substitutional transition metal doping in $MoSi_2N_4$ monolayer: structural, electronic and magnetic properties. *Phys. Chem. Chem. Phys.* **24**, 3035–3042 (2022).
21. Wang, L. et al. Intercalated architecture of MA_2Z_4 family layered van der Waals materials with emerging topological, magnetic and superconducting properties. *Nat. Commun.* **12**, 2361 (2021).
22. Li, S. et al. Valley-dependent properties of monolayer $MoSi_2N_4$, WSi_2N_4, and $MoSi_2As_4$. *Phys. Rev. B* **102**, 235435 (2020).
23. Yao, H. et al. Novel two-dimensional layered $MoSi_2Z_4$ (Z = P, As): New promising optoelectronic materials. *Nanomaterials* **11**, 559 (2021).
24. Yang, C., Song, Z., Sun, X. & Lu, J. Valley pseudospin in monolayer $MoSi_2N_4$ and $MoSi_2As_4$. *Phys. Rev. B* **103**, 035308 (2021).
25. Mortazavi, B. et al. Exceptional piezoelectricity, high thermal conductivity and stiffness and promising photocatalysis in two-dimensional $MoSi_2N_4$ family confirmed by first-principles. *Nano Energy* **82**, 105716 (2021).
26. Nguyen, C., Hoang, N. V., Phuc, H. V., Sin, A. Y. & Nguyen, C. V. Two-dimensional boron phosphide/$MoGe_2N_4$ van der Waals heterostructure: A promising tunable optoelectronic material. *J. Phys. Chem. Lett.* **12**, 5076–5084 (2021).
27. Ai, H. et al. Theoretical evidence of the spin-valley coupling and valley polarization in two-dimensional $MoSi_2X_4$ (X = N, P, and As). *Phys. Chem. Chem. Phys.* **23**, 3144–3151 (2021).
28. Lien, D.-H. et al. Electrical suppression of all nonradiative recombination pathways in monolayer semiconductors. *Science* **364**, 468–471 (2019).
29. Kim, H., Uddin, S. Z., Higashitarumizu, N., Rabani, E. & Javey, A. Inhibited nonradiative decay at all exciton densities in monolayer semiconductors. *Science* **373**, 448–452 (2021).
30. Bernardi, M., Palummo, M. & Grossman, J. C. Extraordinary sunlight absorption and one nanometer thick photovoltaics using two-dimensional monolayer materials. *Nano Lett.* **13**, 3664–3670 (2013).
31. Qiu, D. Y., da Jornada, F. H. & Louie, S. G. Optical spectrum of MoS_2: Many-body effects and diversity of exciton states. *Phys. Rev. Lett.* **111**, 216805 (2013).
32. Marsili, M., Molina-Sánchez, A., Palummo, M., Sangalli, D. & Marini, A. Spinorial formulation of the GW-BSE equations and spin properties of excitons in two-dimensional transition metal dichalcogenides. *Phys. Rev. B* **103**, 155152 (2021).
33. Cho, Y. & Berkelbach, T. C. Environmentally sensitive theory of electronic and optical transitions in atomically thin semiconductors. *Phys. Rev. B* **97**, 041409 (2018).
34. Trolle, M. L., Pedersen, T. G. & Véniard, V. Model dielectric function for 2d semiconductors including substrate screening. *Sci. Rep.* **7**, 39844 (2017).
35. Molina-Sánchez, A., Palummo, M., Marini, A. & Wirtz, L. Temperature-dependent excitonic effects in the optical properties of single-layer MoS_2. *Phys. Rev. B* **93**, 155435 (2016).

36. Carvalho, A., Ribeiro, R. M. & Castro Neto, A. H. Band nesting and the optical response of two-dimensional semiconducting transition metal dichalcogenides. *Phys. Rev. B* **88**, 115205 (2013).
37. Kozawa, D. et al. Photocarrier relaxation pathway in two-dimensional semiconducting transition metal dichalcogenides. *Nat. Commun.* **5**, 4543 (2014).
38. Echeverry, J. P., Urbaszek, B., Amand, T., Marie, X. & Gerber, I. C. Splitting between bright and dark excitons in transition metal dichalcogenide monolayers. *Phys. Rev. B* **93**, 121107 (2016).
39. Wang, G. et al. In-plane propagation of light in transition metal dichalcogenide monolayers: optical selection rules. *Phys. Rev. Lett.* **119**, 047401 (2017).
40. Molina-Sánchez, A., Sangalli, D., Hummer, K., Marini, A. & Wirtz, L. Effect of spin-orbit interaction on the optical spectra of single-layer, double-layer, and bulk MoS_2. *Phys. Rev. B* **88**, 045412 (2013).
41. Molas, M. R. et al. Brightening of dark excitons in monolayers of semiconducting transition metal dichalcogenides. *2D Mater.* **4**, 021003 (2017).
42. Lu, Z. et al. Magnetic field mixing and splitting of bright and dark excitons in monolayer $MoSe_2$. *2D Mater.* **7**, 015017 (2019).
43. Palummo, M., Bernardi, M. & Grossman, J. C. Exciton radiative lifetimes in two-dimensional transition metal dichalcogenides. *Nano Lett.* **15**, 2794–2800 (2015).
44. Chen, H.-Y., Palummo, M., Sangalli, D. & Bernardi, M. Theory and ab initio computation of the anisotropic light emission in monolayer transition metal dichalcogenides. *Nano Lett.* **18**, 3839–3843 (2018).
45. Chen, H.-Y., Jhalani, V. A., Palummo, M. & Bernardi, M. Ab initio calculations of exciton radiative lifetimes in bulk crystals, nanostructures, and molecules. *Phys. Rev. B* **100**, 075135 (2019).
46. Robert, C. et al. Exciton radiative lifetime in transition metal dichalcogenide monolayers. *Phys. Rev. B* **93**, 205423 (2016).
47. Tongay, S. et al. Defects activated photoluminescence in two-dimensional semiconductors: interplay between bound, charged and free excitons. *Sci. Rep.* **3**, 2657 (2013).
48. Linhart, L. et al. Localized intervalley defect excitons as single-photon emitters in WSe_2. *Phys. Rev. Lett.* **123**, 146401 (2019).
49. Kim, J. et al. Observation of ultralong valley lifetime in WSe_2/MoS_2 heterostructures. *Sci. Adv.* **3**, e1700518 (2017).
50. Jauregui, L. A. et al. Electrical control of interlayer exciton dynamics in atomically thin heterostructures. *Science* **366**, 870–875 (2019).
51. Unuchek, D. et al. Room-temperature electrical control of exciton flux in a van der Waals heterostructure. *Nature* **560**, 340–344 (2018).
52. Zhang, C., Wang, H., Chan, W., Manolatou, C. & Rana, F. Absorption of light by excitons and trions in monolayers of metal dichalcogenide MoS_2: Experiments and theory. *Phys. Rev. B* **89**, 205436 (2014).
53. Berkelbach, T. C., Hybertsen, M. S. & Reichman, D. R. Theory of neutral and charged excitons in monolayer transition metal dichalcogenides. *Phys. Rev. B* **88**, 045318 (2013).
54. Dong, S. et al. Direct measurement of key exciton properties: Energy, dynamics, and spatial distribution of the wave function. *Nat. Sci.* **1**, e10010 (2021).
55. Mouri, S. et al. Nonlinear photoluminescence in atomically thin layered WSe_2 arising from diffusion-assisted exciton-exciton annihilation. *Phys. Rev. B* **90**, 155449 (2014).
56. Hoshi, Y. et al. Suppression of exciton-exciton annihilation in tungsten disulfide monolayers encapsulated by hexagonal boron nitrides. *Phys. Rev. B* **95**, 241403 (2017).
57. Erkensten, D., Brem, S. & Malic, E. Exciton-exciton interaction in transition metal dichalcogenide monolayers and van der Waals heterostructures. *Phys. Rev. B* **103**, 045426 (2021).
58. Lee, Y. et al. Boosting quantum yields in two-dimensional semiconductors via proximal metal plates. *Nat. Commun.* **12**, 7095 (2021).
59. Giannozzi, P. et al. QUANTUM ESPRESSO: a modular and open-source software project for quantum simulations of materials. *J. Phys.: Condens. Matter* **21**, 395502 (2009).
60. Perdew, J. P., Burke, K. & Wang, Y. Generalized gradient approximation for the exchange-correlation hole of a many-electron system. *Phys. Rev. B* **54**, 16533–16539 (1996).
61. van Setten, M. J. et al. The pseudodojo: training and grading a 85 element optimized norm-conserving pseudopotential table. *Comput. Phys. Commun.* **226**, 39–54 (2018).
62. Monkhorst, H. J. & Pack, J. D. Special points for Brillouin-zone integrations. *Phys. Rev. B* **13**, 5188–5192 (1976).
63. Marini, A., Hogan, C., Grüning, M. & Varsano, D. Yambo: an ab initio tool for excited state calculations. *Comput. Phys. Commun.* **180**, 1392–1403 (2009).
64. Sangalli, D. et al. Many-body perturbation theory calculations using the Yambo code. *J. Phys.: Condens. Matter* **31**, 325902 (2019).
65. Bruneval, F. & Gonze, X. Accurate GW self-energies in a plane-wave basis using only a few empty states: towards large systems. *Phys. Rev. B* **78**, 085125 (2008).

ACKNOWLEDGEMENTS

M.S. and U.S. acknowledge the King Abdullah University of Science and Technology (KAUST) for funding the research reported in this publication. M.S. thanks Dr. Huabing Shu and Dr. Zhiyong Zhu for helpful discussions. M.R.F. and M.P. acknowledge CINECA for high-performance computing resources under the Iscra-B initiative. M.P. acknowledges funding from Tor Vergata University through the TESLA project and INFN through the TIME2QUEST project.

AUTHOR CONTRIBUTIONS

M.S. executed the calculations under the guidance of M.P. M.R.F. and M.S. drafted the manuscript and prepared the figures. All authors contributed to the evaluation of the results and contributed to the final version of the manuscript.

COMPETING INTERESTS

The authors declare no competing interests.

ADDITIONAL INFORMATION

Supplementary information The online version contains supplementary material available at https://doi.org/10.1038/s41699-022-00355-z.

Correspondence and requests for materials should be addressed to Udo Schwingenschlögl or Maurizia Palummo.

Reprints and permission information is available at http://www.nature.com/reprints

Publisher's note Springer Nature remains neutral with regard to jurisdictional claims in published maps and institutional affiliations.

Open Access This article is licensed under a Creative Commons Attribution 4.0 International License, which permits use, sharing, adaptation, distribution and reproduction in any medium or format, as long as you give appropriate credit to the original author(s) and the source, provide a link to the Creative Commons license, and indicate if changes were made. The images or other third party material in this article are included in the article's Creative Commons license, unless indicated otherwise in a credit line to the material. If material is not included in the article's Creative Commons license and your intended use is not permitted by statutory regulation or exceeds the permitted use, you will need to obtain permission directly from the copyright holder. To view a copy of this license, visit http://creativecommons.org/licenses/by/4.0/.

© The Author(s) 2022